Direct Observation of Nanoparticle–Cancer Cell Nucleus Interactions

Duncan Hieu M. Dam,[†,∥] Jung Heon Lee,[†,⊥,∥] Patrick N. Sisco,[†] Dick T. Co,[†] Ming Zhang,[§] Michael R. Wasielewski,[†] and Teri W. Odom[†,‡,*]

[†]Department of Chemistry and [‡]Department of Materials Science and Engineering, Northwestern University, Evanston, Illinois 60208, United States, [§]Department of Molecular Pharmacology and Biological Chemistry, Northwestern University, Chicago, Illinois 60611, United States, and [⊥]School of Advanced Materials Science and Engineering, Sungkyunkwan University (SKKU), Suwon, South Korea 400-746. [∥]These authors contributed equally to the work.

ABSTRACT

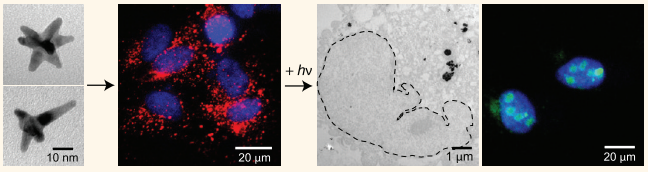

We report the direct visualization of interactions between drug-loaded nanoparticles and the cancer cell nucleus. Nanoconstructs composed of nucleolin-specific aptamers and gold nanostars were actively transported to the nucleus and induced major changes to the nuclear phenotype *via* nuclear envelope invaginations near the site of the construct. The number of local deformations could be increased by ultrafast, light-triggered release of the aptamers from the surface of the gold nanostars. Cancer cells with more nuclear envelope folding showed increased caspase 3 and 7 activity (apoptosis) as well as decreased cell viability. This newly revealed correlation between drug-induced changes in nuclear phenotype and increased therapeutic efficacy could provide new insight for nuclear-targeted cancer therapy.

KEYWORDS: gold nanoparticles · aptamers · nucleolin · drug delivery · light-triggered release · nanoparticle–nucleus interactions

The nucleus is the most important organelle in the growth, proliferation, and apoptosis of a cell.[1,2] Controlling the processes governed by the nucleus has been a primary goal for nuclear-targeted cancer therapy.[3,4] Conventionally, viral vectors are used to deliver drugs to cell nuclei,[5] but a drawback is the resulting immunogenic response.[6,7] Nanomaterials are promising delivery vehicles because drugs can be densely loaded on the nanoparticle (NP), which simultaneously enhances the stability and pharmacokinetics of the molecules *in vitro*.[8] Recently, nuclear targeting by peptide-modified gold NPs has seen some success[9,10] and shown improved anticancer efficacy;[11] however, the mechanism responsible for the increased cell death is unknown because no *nanoscale* direct visualization of how the NPs affected the nucleus was shown.

Nucleolin is the most abundant nucleolar phosphoprotein in the nucleus of normal cells[12,13] but in metastatic and rapidly dividing cells is overexpressed in the cytoplasm and translocated to the cell membrane.[14−16] The trafficking ability of nucleolin has been implicated in transporting anticancer ligands from the cell surface to the nucleus.[16,17] Recently, the single-stranded DNA aptamer AS1411 (26 mer, 7.8 kDa) has been tested as a chemotherapeutic agent because of its ability to bind to nucleolin with a high binding affinity (K_d is in the picomolar to low nanomolar range).[17−20] By blocking several functions of nucleolin, AS1411 can result in the arrest of DNA repair in the nucleus as well as destabilize bcl-2 mRNA to result in tumor cell death.[14,18] This paper reports the direct visualization of a two-component nanoconstruct—AS1411 (Apt) and gold nanostars (AuNS)—interacting with cancer cell nuclei. We exploited the shuttling properties of nucleolin to traffic the nanoconstructs (Apt–AuNS) to the perinuclear region (Figure 1) and then tested how nuclei–nanoconstruct interactions correlated with cell activity.

RESULTS AND DISCUSSION

Two-Component Nanoconstructs Whose Surface Ligands Are Also Drugs. We synthesized biocompatible AuNS by reducing Au(III) chlorate with 4-(2-hydroxyethyl)-1-piperazineethanesulfonic acid (HEPES), one of the Good's buffers used in cell culture.[21] By controlling the ratio of the Au(III) salt to HEPES, we produced nanostars with average sizes around 25 nm (Figure 2A,B). Despite this small size, AuNS supported a localized surface plasmon (LSP) resonance centered at 780 nm, within the biologically transparent near-infrared (NIR) spectral window (Figure S1A in Supporting Information) because of

* Address correspondence to todom@northwestern.edu.

Received for review January 20, 2012 and accepted March 16, 2012.

Published online March 16, 2012
10.1021/nn300296p

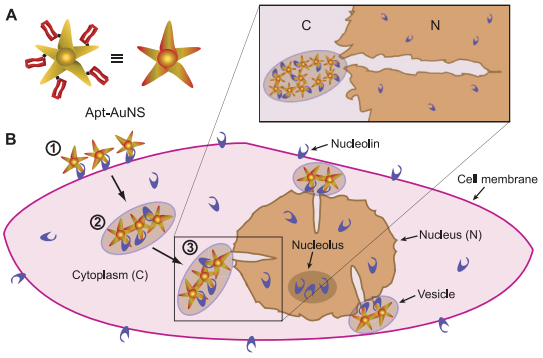

Figure 1. Nucleolin-mediated, active trafficking of nanoconstructs to the cancer cell nucleus. (A) Scheme of a two-component nanoconstruct (Apt–AuNS) consisting of nucleolin-specific aptamers AS1411 and a gold nanostar (AuNS). (B) Scheme depicting delivery to the nucleus *via* three major steps: (1) binding of Apt–AuNS to surface nucleolin receptors; (2) shuttling of Apt–AuNS by nucleolin to locations near the cell nucleus; and (3) interactions with the nuclear envelope (NE) of the nucleus. (Inset) Apt–AuNS interactions with the nucleus result in deep, intruding folds of the NE into the nucleoplasm.

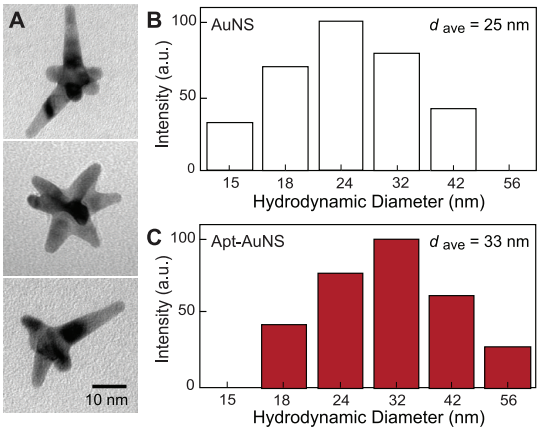

Figure 2. Surface functionalization and trafficking properties of nanoconstruct. (A) TEM images of biocompatible AuNS. Hydrodynamic diameter of AuNS (B) before (as-synthesized) and (C) after conjugation with AS1411 aptamer measured by dynamic light scattering.

its multibranched shape. We grafted AS1411 aptamer to AuNS to create Apt–AuNS nanoconstructs by replacing the HEPES capping molecules with thiolated aptamers according to published protocols.[22] To determine the number of aptamers attached to each AuNS, we compared differences in fluorescence intensity of a solution of Cy5-labeled aptamer before and after conjugating the AuNS. We estimated that each AuNS supported approximately 950 AS1411 strands, which is in agreement with the theoretical calculation using the method reported by Ma *et al.*[23] Dynamic light scattering of the Apt–AuNS nanoconstructs showed an increase in hydrodynamic diameter from 25 to 32 nm (Figure 2C). This 3.5 nm increase in radius is consistent with the length of the aptamer dimer; circular dichroism measurements confirmed that the G-quadruplexes were still formed in the Apt when attached to the AuNS (Figure S1B). We also prepared a control nanoconstruct (cApt–AuNS), where the cApt had a cytosine-rich, nonquartet DNA structure (Figure S1C). This control sequence was selected because of its low affinity to nucleolin.[18,19]

Nucleolin Can Traffic the Nanoconstruct to the Perinuclear Region. As a first test of the trafficking properties of nucleolin for Apt–AuNS, we incubated Cy5-labeled nanoconstructs (Cy5–Apt–AuNS) with HeLa cervical cancer cells for confocal fluorescence microscopy analysis. In these experiments, the Cy5-label was at the 3′-end of the aptamer so that fluorescence quenching by the AuNS would be minimized. Confocal images showed that the fluorescence signals of the Cy5–Apt–AuNS overlapped with the DAPI-stained nucleus as the incubation time increased from 5 to 24 h (Figure 3A–D). In contrast, there was little colocalization between the Cy5 and DAPI signals when HeLa cells were treated with cApt–AuNS for the same incubation times (Figure 3E–H). These results suggest that the nanoconstructs were trafficked by nucleolin near the cell nucleus, which is consistent with observations of nuclear targeting by peptides by other far-field imaging tools such as differential interference contrast microscopy and dark-field scattering.[9–11] Actin-mediated nucleolin transport or lysosomal delivery of the Apt–AuNS could possibly be responsible for how shuttling to the perinuclear region occurs;[24,25] however, there are few studies identifying the former mechanism, and the latter is not consistent with the confocal data in Figure 3. Although 24 h incubation times showed the highest concentration of particles near the nucleus, we chose 7 h incubation times for the remainder of the experiments to avoid any potential complexities with cell cycle phases.[26]

Although light-based imaging can provide diffraction-limited information on the locations of NPs within cells, they cannot visualize effects of nanoconstructs on cellular compartments at the nanometer scale; however, high-resolution transmission electron microscopy (HRTEM) can resolve interactions at the 10 nm level. Figure 4A shows that, after 7 h of incubation with HeLa cells, clusters of Apt–AuNS were localized in the cytoplasm (C) and very close to the nucleus (N). In contrast, only a few clusters of cApt–AuNS were observed near the nucleus, and these images were acquired only after extensive searching (Figure 4B). To confirm that uptake and transport of the Apt–AuNS nanoconstructs in cancer cells was mediated by nucleolin, we carried out control experiments using MCF-10A, a normal mammary epithelial cell line lacking surface nucleolin,[18] and OVCAR-3, an ovarian carcinoma cell line with low expression of surface nucleolin (data not shown). After 7 h of incubation, we found only a minimal number of Apt–AuNS anywhere inside the MCF-10A cells (Figure 4C) and only a few Apt–AuNS inside OVCAR-3 cells (Figure 4D).

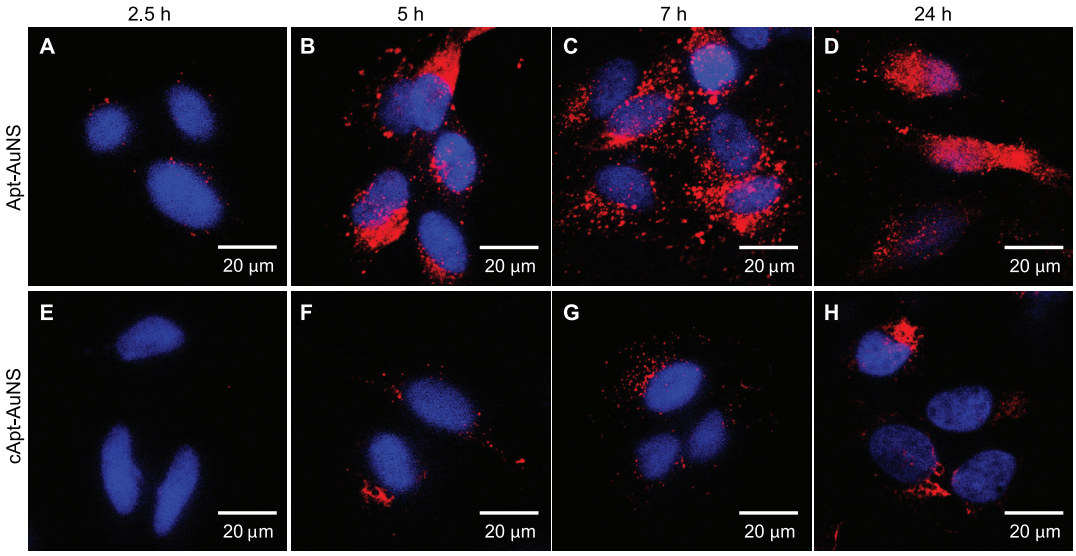

Figure 3. Intracellular trafficking of nanoconstructs to the nucleus. Intracellular delivery of Apt–AuNS to the nucleus was monitored by incubating HeLa cells with Cy5–Apt–AuNS and imaging with a confocal fluorescence microscope. (A–D) Accumulation of Cy5–Apt–AuNS in the nucleus, indicated by the red fluorescence, starts to appear after 5 h and increased significantly after 7 and 24 h. This observation suggests that Apt–AuNS are internalized by HeLa cells and are transported to locations spatially close to the nuclei. (E–H) When HeLa cells are treated with control nanoconstructs (Cy5–cApt–AuNS), the Cy5 signal is only observed in the cytoplasm but not in the cell nucleus.

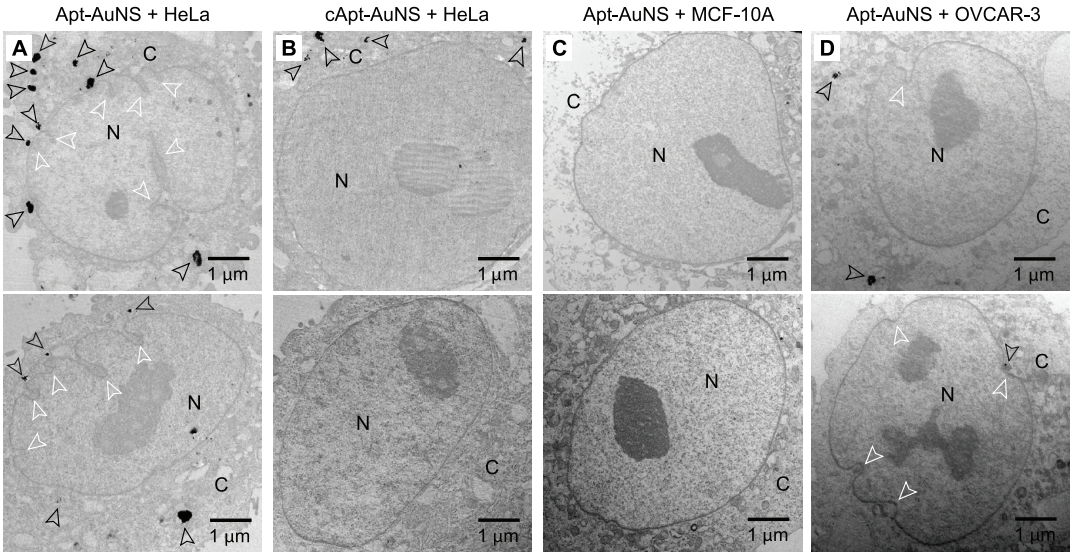

Figure 4. Nuclear envelope invaginations in cancer cell nuclei at locations near Apt–AuNS. TEM images of (A) Apt–AuNS-treated HeLa cells show mechanical deformation of the NE generated by the nanoconstructs. (B) Nuclei of cApt–AuNS-treated HeLa cells and (C) Apt–AuNS-treated MCF-10A cells appear undisturbed. (D) Fewer Apt–AuNS and NE folds are observed in OVCAR-3 cells. All cells were incubated for 7 h with the nanoconstructs. White arrows highlight the locations of the NE folds, and the black arrows point to the Apt–AuNS clusters.

Nanoscale Imaging of Nanoconstruct–Nucleus Interactions Reveals NE Folding at the Location of the Nanoconstruct. Surprisingly, high-resolution TEM images showed major changes in nuclear phenotype near the site of the nanoconstruct; the nuclear envelope (NE) was extremely deformed in over 60% of the HeLa cells with nanoconstructs. Our analysis of over 150 cells showed an average of 3 ± 0.5 folds per nucleus after the cancer cells were incubated with Apt–AuNS for 7 h. There have only been some reports on NE folding[27] and only a few because of the presence of a drug.[28] More importantly, the locations of over 80% of the intruding folds into the nucleoplasm correlated directly with the location of the Apt–AuNS near the nucleus. We analyzed >100 cell sections to confirm the spatial correlation between the position of the vesicles containing Apt–AuNS and the sites of folding in the NE. Ninety percent of nanoconstructs or clusters were located either within 1.5 ± 0.5 μm from the opening of the nuclear membrane folds or inside the folds

(Figure S2), which strongly implies that the presence of the nanoconstruct produced the localized changes in the cancer cell NE. We also observed that 20% of the NE invaginations did not have Apt−AuNS near them. However, considering that the thickness of the section is only 80−90 nm, it is possible that the TEM sections that show NE invaginations without particles are also generated by Apt−AuNS. This interpretation is consistent that the nucleus is a 3D object but that TEM can only image in 2D—so, the Apt−AuNS are needed for the NE folds, but they can only be imaged in other TEM sections. In addition to our analysis, we found that increased incubation times of the nanoconstruct resulted in even deeper invaginations or multibranched folds of the NE at 7 h. Cross sections of these deep folds within the nucleoplasm were even observed at 24 h (Figure S3). We conducted statistical analysis over 30 different cells in each set of samples and observed that the length of the NE folds increased from 1.2 ± 0.1 μm after 7 h incubation to 1.4 ± 0.1 μm after 24 h incubation ($p < 0.01$). We also observed folding in the NE in OVCAR-3 cells; however, there were far fewer folds (1 ± 0.5 folds per nucleus, $p < 0.001$) compared to that in HeLa cells (Figure 4E).

Since NE folding was only observed in cancer cells treated with Apt−AuNS but not cApt−AuNS, we hypothesized that the AS1411 aptamers were primarily responsible for NE folding. Surprisingly, there have been no reports on the possible changes in nuclear phenotype induced by AS1411 despite this drug being in phase II clinical trials.[29] We conducted experiments with free AS1411 and observed NE folding in *ca.* 70% of the HeLa cell population after treatment at therapeutic concentrations (10 μM)[18] (Figure S4A). Surprisingly, if we used 450 nM free AS1411—the equivalent of AS1411 concentration in 0.3 nM of Apt−AuNS—there was no morphological change in the cancer cell nucleus compared to treatment with 0.3 nM Apt−AuNS (Figure S4B). This finding highlights the role that AuNS serves as a carrier of high, local concentrations of aptamer that can be delivered near the nucleus. There is the possibility that ligand-induced nucleolin clustering as a result of Apt−AuNS binding to multiple nucleolin proteins could also result in NE folding. In contrast, and in agreement with cApt−AuNS results, we found no deformations in the nucleus after treatment with free control aptamer (10 μM, Figure S4C). Altogether, these results indicate that the interactions between Apt−AuNS vesicles and the cell nucleus are mediated by AS1411. How nucleolin and AS1411 aptamers inside vesicles interact, however, is not well-understood. A recent report suggests that uptake of AS1411 is *via* macropinocytosis, resulting in macropinosomes, which are leakier than endosomal vesicles.[30] Further study is needed to elucidate details of this uptake mechanism.

Light-Triggered Release of Aptamers Induces Further Changes to Nuclear Phenotype. To test whether the concentrated release of aptamer from the constructs could increase NE folding further, we detached AS1411 from the AuNS surface using femtosecond (fs) pulses at the LSP wavelength of the AuNS (Materials and Methods). Ultrafast pulses at NIR wavelengths have been used to detach thiolated DNA from gold nanoparticles while still maintaining the viability of the molecules.[31,32] We identified the optimal irradiation conditions (*e.g.*, shortest excitation time, lowest pulse energy) using Cy5-labeled Apt−AuNS incubated with HeLa cells for 7 h. For these experiments, the Cy5 was situated at the thiol end of the aptamer (closest to the AuNS surface, Apt−Cy5−AuNS) so that only if the AS1411 aptamer was released from the AuNS would Cy5 fluorescence be observed. In buffer, we found that 40 fs pulses (power density 4.8 W/cm^2), irradiation times of 2 s, and a wavelength of 800 nm produced the largest fluorescence signal and the highest amount of AS1411 release (Materials and Methods). This exposure time is much shorter than previous reports that required an average of a few minutes of NIR irradiation.[31,33,34] Flow cytometry of HeLa cells and Apt−Cy5−AuNS irradiated with NIR fs pulses showed a significant increase in Cy5 fluorescence intensity compared to nonirradiated samples (Figure S5A). These data confirmed that fs-NIR irradiation was able to release the aptamer from AuNS in cells.

HRTEM images also revealed that the nanoconstructs were in some type of vesicle throughout the intracellular trafficking process (Figure 5A). Femtosecond excitation produced a breaking up of the clusters of Apt−AuNS (Figure 5B), partial deterioration of the membrane, and release of the aptamer from the AuNS. Possible heating effects cannot be eliminated, but reports suggest that this temperature increase is minimal.[31,32] Second, >95% of the cells containing Apt−AuNS showed deformations in nuclear phenotype and NE invaginations (5 ± 0.5 folds per nucleus) immediately after irradiation (Figure 5C). This 40% increase in the number of cells that show NE folding (compared to 60% without released aptamer) suggests that the released aptamers increase the effects of aptamer−NE interactions. We studied the effects of the released drug over longer times by examining the cancer cell nucleus at 24, 48, and 72 h after aptamer release. At 24 and 48 h time points, the NE invaginations became deeper (1.5 ± 0.1 and 1.9 ± 0.3 μm, respectively ($p < 0.001$)) (Figure 5D,E). After 72 h, 98% of the cell population was composed of small daughter cells that showed extreme NE roughening (Figure 5F). These observations suggest that the released AS1411 continues to have an effect even after 72 h.

Extent of Nuclear Envelope Deformation Correlates to Cellular Activity. Direct comparison of the HeLa cell nuclei before and after fs irradiation indicates that an increase in the number of NE folds (>2 times) was observed immediately after the AS1411 was released from the

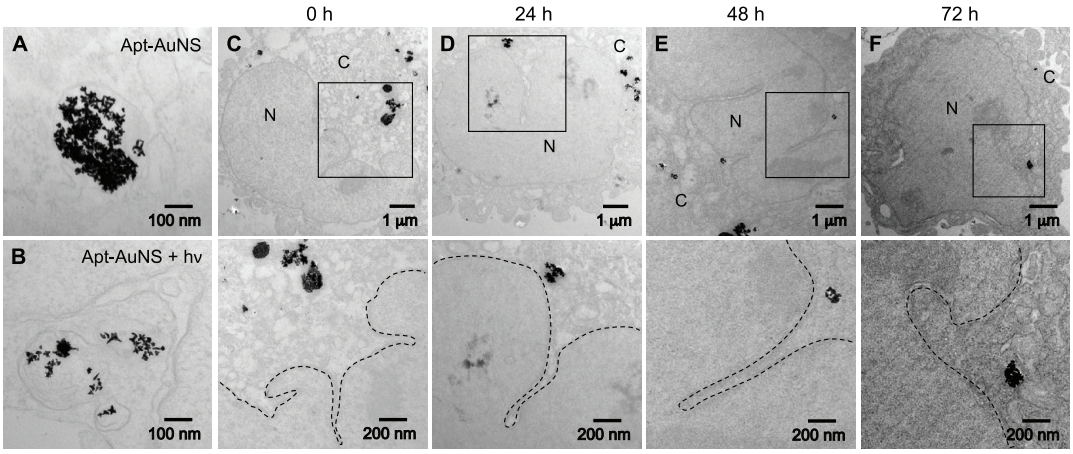

Figure 5. Number of NE folds in a nucleus increases when aptamers are released from the nanoconstructs by fs pulsed light. (A) TEM image depicts that the vesicle membrane surrounding the Apt–AuNS clusters conforms to the particles and is intact. (B) Vesicle membranes are partially deteriorated after irradiation with 2 s of fs pulsed light, which facilitates escape of aptamers from the vesicle. The morphology of the AuNS does not change significantly after light irradiation. (C–F) Nuclei of HeLa cells treated with 0.3 nM of Apt–AuNS for 7 h and followed by 2 s of fs pulsed irradiation show large changes in nuclear phenotype and an increase in number of NE folds (C) immediately, (D) at 24 h, (E) at 48 h, and (F) at 72 h after the aptamers were released.

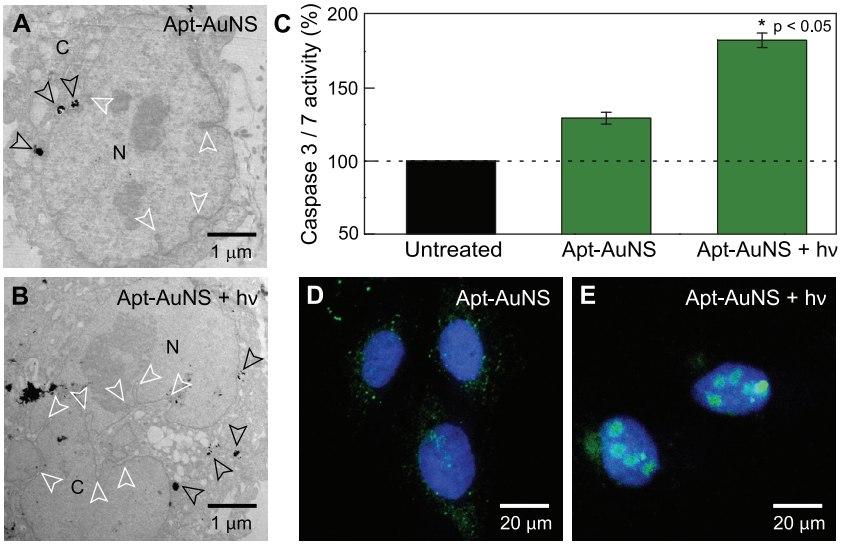

Figure 6. Nuclear phenotype and biological activity of the nucleus are correlated. (A) TEM image of a HeLa nucleus treated with Apt–AuNS showing a small number of NE folds after incubation for 7 h. (B) TEM image showing a dramatic increase in the number and depth of the NE invaginations after fs pulsed irradiation for 2 s. White arrows highlight the locations of the NE folds, and the black arrows point to the Apt–AuNS clusters. (C) Caspase 3 and 7 activity of Apt–AuNS-treated HeLa cells increased by 1.5 times immediately post-irradiation ($p < 0.05$). (D,E) Confocal fluorescence images of double-stranded DNA breaks (DSBs) indicated by the green FITC fluorescence in HeLa cells incubated with (D) Apt–AuNS only and (E) Apt–AuNS and light-triggered release of aptamer. Although both treatments result in DSBs, there are more DSB foci after the aptamers are released from the AuNS, which produces more severe changes in nuclear phenotype.

AuNS (Figure 6A,B). To test whether these physical changes were correlated with cell function, we measured caspase 3 and 7 activities (Materials and Methods) since an increase in caspase activity suggests that cells are undergoing apoptosis.[3] Figure 6C shows that the caspase activity of HeLa cells treated with Apt–AuNS + $h\nu$ increased immediately by 1.5 times compared to cells incubated with only Apt–AuNS. In addition, since apoptosis is related to the functional disruption of the nucleus,[11] the amount of double-stranded DNA breaks (DSBs) was evaluated by confocal fluorescence microscopy. Figure 6D,E shows that DAPI-stained nuclei overlapped with the green FITC fluorescence of the DSB foci (Materials and Methods). Clearly, the DSB foci exhibited significantly higher FITC signals after aptamer release from the AuNS carriers (Figure 6E). Therefore, the increases in caspase activity as well as the increase in DNA damage are highly correlated to the increased levels of NE deformation.

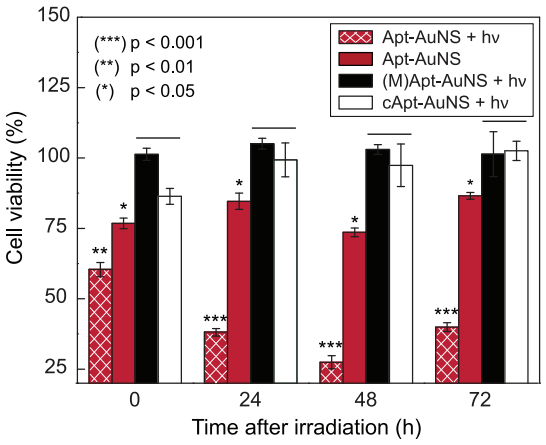

Figure 7. Increase in the extent of NE folding is related to metabolic shutdown and cell death. Viability analysis of Apt–AuNS-treated HeLa cells shows a maximum decrease (>70%) between 24 and 72 h after light-triggered release of the aptamer ($p < 0.001$). Even without released aptamer, Apt–AuNS-treated cells showed a decrease in viability of 25%. Minimum cell death was observed in cApt–AuNS-treated HeLa cells (cApt–AuNS + $h\nu$) and Apt–AuNS-treated MCF-10A cells ((M)Apt–AuNS + $h\nu$) after the 2 s irradiation. Lines over bars indicate groups that are not significantly different.

Finally, we investigated whether the physical deformation of the NE correlated with changes in cellular activities such as metabolism. Cell viability was measured since a decrease in viability would indicate shutdown of metabolic activity.[3] We found that HeLa cells treated with both Apt–AuNS only and Apt–AuNS + $h\nu$ showed decreased cell viability over 72 h. Consistent with the increased amounts of NE folding, 40% of the HeLa cell population treated with Apt–AuNS + $h\nu$ died immediately, while only 25% of the population died with Apt–AuNS (Figure 7).

This result confirms that locally increasing the availability and concentration of the AS1411 near the cell nucleus can have deleterious effects on the metabolic activity of the cells ($p < 0.01$) and result in cell death. Furthermore, viability analysis showed that >70% of the cell population died between 48 and 72 h after release of the aptamer, a percentage that is much higher than that of Apt–AuNS only treated cells.

In addition, the viabilities of cApt–AuNS-treated HeLa cells and Apt–AuNS-treated MCF-10A cells after ultrafast light irradiation were nearly 100%, which is expected since the nuclei of these cells remained intact (Figure 4C,D), and the 2 s irradiation did not damage the cells (Figure S5B). These results strongly suggest that the physical deformation of the nucleus can be related to prolonged shutdown of cellular metabolism. Finally, we observed that the viability of cells treated with 450 nM of free aptamer (the estimated concentration based on the number of aptamers on each AuNS and the concentration of AuNS) was much higher than for cells treated with Apt–AuNS + $h\nu$ (Figure S8). Therefore, the localized release of high concentrations of aptamer from the AuNS surface in the perinuclear region can have a significant effect on therapeutic efficiency.

CONCLUSION

In summary, we have directly visualized the interaction between a drug-loaded nanoconstruct and the cancer cell nucleus and correlated the resulting morphological deformations in the NE with increased efficacy. By taking advantage of the shuttling protein nucleolin, we could actively deliver the nanoconstruct to locations in nanoscale proximity to the nucleus, which resulted in extreme deformation and invagination of the NE at the site of the construct. These morphological changes were exacerbated upon ultrafast, light-triggered release of the aptamer from the AuNS. That cancer cell function can be correlated with deformations in the nucleus suggests that major challenges in particle-based, nuclear-targeted therapy can be overcome. For example, complete internalization of nanoconstructs inside the nucleus is not necessary if induced physical changes in nuclear phenotype can disrupt nuclear functions. Also, because morphological effects are induced by NPs outside the nucleus, there may be no limitation in the size or shape of NPs that can achieve a similar response. These factors should provide insight into the development of new strategies to design drug-loaded NPs with increased therapeutic efficacy.

MATERIALS AND METHODS

Synthesis of Gold Nanostars. Gold nanostars (AuNS) were synthesized by reducing Au(III) chlorate in HEPES buffer to create biocompatible, surfactant-free gold nanoparticles for *in vitro* studies.[21] The AuNS were prepared by mixing 5 μL of 40 mM $HAuCl_4$ (Sigma Aldrich) with 1 mL of 140 mM HEPES buffer. The resonance wavelength of the AuNS was measured using UV–vis spectroscopy. Particle size was determined using both high-resolution transmission electron microscopy (HRTEM) and dynamic light scattering (DLS).

Preparation of Apt–AuNS Nanoconstructs. AS1411 aptamer with a disulfide modification at the 5′-end (5′-T-(C6-S-S-C6)-TTG GTG GTG GTG GTT GTG GTG GTG GTG G-3′) and a control aptamer (cApt), where all the guanines were replaced with cytosines (5′-T-(C6-S-S-C6)-TTC CTC CTC CTC CTT CTC CTC CTC CTC C-3′), were purchased from TriLink Biotechnologies, Inc. HPLC-purified aptamers were dissolved in Millipore water (18.2 MΩ·cm) to make 1 mM solutions. The disulfide bond was cleaved by adding 2.5 μL of 25 mM tris(2-carboxyethyl)phosphine (TCEP) (Sigma Aldrich) to 10 μL of the 1 mM aptamer solution. After 30 min, the thiolated aptamer solution was added to 10 mL of 0.2 nM solution of AuNS and left overnight to form the nanoconstruct (Apt–AuNS). To increase the surface concentration of aptamers on AuNS,[35] we salted the mixture solution with 2.5 mL of a 500 mM solution of NaCl twice, separated by 4 h. The size of the nanoconstructs was characterized using DLS.

Calculation of the Number of Aptamers per AuNS. Cy5-labeled aptamer (5′-T-(C6-S-S-C6)-TTG GTG GTG GTG GTT GTG GTG GTG GTG G-Cy5-3′) was used to estimate the number of aptamers

functionalized on a single AuNS. Cy5 was placed at the 3′-end of the aptamer, while the 5′-end was attached to the AuNS surface *via* the gold−sulfur bond. To estimate the number of aptamers involved in the AuNS functionalization, we took fluorescence measurements of the free Cy5-labeled aptamers in the solution before the conjugation. Cy5-labeled aptamers were then conjugated on AuNS based on aforementioned protocol. After 24 h, the nanoconstruct solution was centrifuged at 15 000 rpm for 11 min, and the supernatant was collected. The fluorescence of the supernatant was measured to determine the amount of aptamers which did not react with the AuNS. Upon the basis of these results, there are approximately 950 AS1411 strands functionalized on a single AuNS.

Tissue Culture for Cancer and Control Cell Lines. The human cervical carcinoma HeLa cell line (ATCC) was maintained in DMEM medium (Gibco) supplemented with 10% fetal bovine serum (FBS) (Invitrogen). The human epithelial cell line MCF-10A (ATCC) was maintained in DMEM/F12 medium (Gibco) supplement with 10% horse serum (Invitrogen), 20 ng/mL epidermal growth factor (EGF) (Sigma Aldrich), 0.5 mg/mL hydrocortisone (Sigma Aldrich), 100 ng/mL cholera toxins (Sigma Aldrich), and 10 μg/mL insulin (Sigma Aldrich). The ovarian carcinoma cell line OVCAR-3 (ATCC) was maintained in RPMI-1640 medium (Gibco) supplemented with 20% fetal bovine serum (Invitrogen) and 0.01 mg/mL bovine insulin (Sigma Aldrich). The cells were cultured at 37 °C with 5% CO_2 and plated in T25 flasks (VWR) with aforementioned media.

Confocal Imaging of Dye-Labeled Nanoconstructs. HeLa cells (2×10^4 cells/coverslip) were plated on poly-L-lysine-treated coverslips and maintained with Dulbecco modified Eagle's medium (DMEM) with 10% fetal bovine serum (FBS). After cell growth (37 °C in 5% CO_2) for 24 h, the growth medium was removed, and the cells were washed three times with phosphate buffered saline (PBS) (Invitrogen). Then, 300 μL of 0.3 nM 3′-labeled Cy5−Apt−AuNS in DMEM was added to cells for different incubation times (2.5, 5, 7, and 24 h). For the control, 0.3 nM of nontargeting 3′-labeled Cy5−cApt−AuNS was added to HeLa cells for similar incubation times. After the AuNS solutions were removed, the cells were washed three times with PBS. Then, 200 μL of 4% paraformaldehyde (Sigma Aldrich) was added for 20 min to fix the cells, followed by washing the samples three times with PBS. A drop of ProLong Gold antifade reagent with DAPI (Invitrogen) was added to each well, and then the sample was mounted on a glass slide for fluorescence imaging.

TEM Imaging of Nanoconstructs and Cancer Cells. HeLa cells were plated at 2×10^5 cells per well in a 12-well plate for 24 h. After removal of the growth media, 3 mL of the 0.3 nM Apt−AuNS in DMEM was added to each well for 2, 5, 7 and 24 h incubation. HeLa cells were harvested by treating with 0.25% trypsin-EDTA for 5 min at 37 °C in 5% CO_2. The cells were then centrifuged at 500*g* for 5 min. The supernatant was removed, and the pellets were resuspended and washed in PBS. The cells were fixed by the first infiltration step using a Pelco Biowave microwave. Two exchanges of the primary fixative were made using 2% paraformaldehyde and 2.5% glutaraldehyde in a 0.05 M sodium phosphate buffer followed by two buffer washes. The secondary fixative of 1.5% osmium tetroxide in DI water was followed by two DI water rinses. Acetone was used for the dehydration series and infiltration steps. The EMBed 812 resin was made to medium hardness. Bench infiltration steps at room temperature included resin to acetone ratios of 1:1 for 4 h and 2:1 overnight, followed by 100% resin for 3 h, and 100% resin for another hour. Polymerization took place in a 60 °C oven for 24 h, and no additional staining was done. A Leica Ultracut S or RMC MT-6000 XL microtome was used to collect 90 nm thick sections. Cell sections were imaged and captured by a JEOL1230 TEM and Gatan 831 bottom-mounted CCD camera.

Statistical Analysis of the Nuclear Envelope Folds. The number of NE folds was averaged over 150 cell sections based on TEM images. The lengths of the NE folds were measured using the measuring tool in the Gatan 831 bottom-mounted CCD camera software. The reported lengths were averaged over 30 cell sections of each sample group. The standard error of the mean, defined as the standard deviation of the sampling distribution, was reported. We performed two-way ANOVA (Origin, 8th ed.) of the distances of Apt−AuNS from the cell nucleus and the lengths of NE folds between two sample groups and tested against the null hypothesis that there is no difference in distance or length between the two groups.

Ultrafast Light-Triggered Release of Aptamers from AuNS. The femtosecond NIR pulses used in the irradiation experiments were generated using a 1 kHz Ti:sapphire regenerative amplifier (Spitfire Pro, Spectra-Physics) seeded by a Ti:sapphire oscillator (Tsunami, Spectra-Physics). The center wavelength was set to 800 nm, and the pulse duration was 40−50 fs. The beam was focused to a 4.5 mm diameter spot at the sample using a 50 cm focal length plano-convex lens. The average pump power was attenuated to 760 mW, corresponding to a power density of 4.8 W/cm^2, using a gradient neutral density filter wheel. Samples were irradiated in the 96-well plates, and the irradiation time was controlled to within 2 ms by a shutter (Uniblitz, Vincent Associates) connected to a computer.

Release of Aptamers from AuNS in Phosphate Buffer Saline (PBS). Eighty microliters of 0.2 nM Apt−Cy5−AuNS in PBS was added in each of a 96-well plate. The Cy5 dye was located at the 5′-end of aptamer which also contains a thiolated group attaching to the AuNS (5′-T-(C6-S-S-C6)-Cy5-TTG GTG GTG GTG GTT GTG GTG GTG GTG G-3′). Because the dye was closest to the surface of the particle (<1 nm), we expected the fluorescence would be quenched by the gold.[36] Each well was irradiated ($h\nu$) for 2 s using a 40 fs, 1 kHz repetition rate, 800 nm pulsed laser at different power densities (from 0.5 to 4.8 W/cm^2), and the fluorescence was measured using a PC1 fluorimeter. We then determined the fluorescence intensity of the solution with all of the thiolated Cy5-labeled aptamer replaced from AuNS with mercaptobutanol in order to calculate the percentage of released aptamer from fs irradiation.[22] Our results showed that approximately 20% of the DNA was released from the AuNS after fs irradiation at 4.8 W/cm^2 for 2 s.

Intracellular Release of Aptamers from AuNS. HeLa cells were plated at 10×10^3 per well in 48 wells of a 96-well plate for 24 h. After removal of the growth media from the wells, 100 μL of 0.3 nM Apt−Cy5−AuNS in RPMI-1640 colorless media was added to each well and incubated for 7 h. Half of the wells were subjected to 2 s irradiation at 4.8 W/cm^2 (same conditions as in buffer), while the other half were untreated to serve as a control. Apt−AuNS HeLa cells were then collected by trypsinization (5 min) of the cells from the plate and spun down (350*g*) for 5 min to form a cell pellet. The pellets were resuspended and washed twice in PBS, after which PBS was removed and replaced with binding buffer (Invitrogen). The fluorescence signal measured by flow cytometry showed an increase by 2 times in fs irradiated cells.

Measurement of Caspase 3/7 Activity. Apo-ONE Homogeneous Caspase-3/7 assay kit (Promega) was used to test caspase 3/7 activity, an apoptotic indicator, in cancer cells after light-triggered release of Apt. The assay was performed following the protocol by Promega.[36] The cells were plated on a 96-wells plate (~10 000 cells/well) for 24 h. After treatment, the cells were lysed with the mixture containing pro-fluorescence substrate (Z-DEVD-R110) and bifunctional cell lysis/activity buffers. We measured the caspase 3/7 activity using Synergy 3 microplate reader (NU-HTA) to determine the fluorescence intensity of R110 ($487_{ex}/528_{em}$ nm) at different time points (0, 24, 48, and 72 h) after release of the aptamer. Error bars were calculated by taking the ratio between standard deviation of the sample set and square root of the sample population ($N = 18$). Two-way ANOVA was performed (Origin, 8th ed.) to evaluate significant differences between the factor level means within a factor and for interactions between the factors of different sample sets.

Determination of Double-Stranded DNA Breaks (DSBs) in the Cell Nucleus. DSBs were determined by immunostaining of serine-139 phosphorylated γ-H2AX protein with the primary antibody anti-γ-H2AX (Sigma Aldrich).[37] The secondary antibody, goat anti-mouse IgG labeled with the green fluorescent dye FITC (Millipore), was attached to the primary antibody. dsDNA breaks were indicated by the bright green FITC signals. HeLa cells (2×10^4 cells/coverslip) were plated on poly-L-lysine-treated coverslips. After treatment, the cells were fixed with 4% paraformaldehyde for 20 min. The fixed cells were then incubated with

1 mL of PBS for 5 min and then treated with 300 μL of PBS containing 0.5% Triton X-100 (Invitrogen) for 3 min to enhance permeability. The cells were washed with PBS three times and incubated with primary antibody anti-γ-H2AX diluted in 1% Tween-PBS (T-PBS) solution containing 0.1% BSA (1:100) for 1 h. The cells were then washed with PBS three times and incubated with secondary antibody diluted in T-PBS (1:250) for 20 min. A drop of ProLong Gold antifade reagent with DAPI (Invitrogen) was added to the coverslip, and the sample was then placed on a glass slide for confocal fluorescence imaging.

Measurement of Cell Viability. Cell-Titer Blue Cell viability assay (Promega) was used to determine the viability of cells. This kit contains highly purified nonfluorescent rezasurin in buffer. Viable cells will reduce rezasurin to resofurin, which is a highly fluorescent molecule. Nonviable cells, however, lose their metabolic activity and will not reduce rezasurin. Cells were plated on a 96-well plate (~10 000 cells/well) for 24 h. After treatment, we determined cell viability by measuring the fluorescence intensity (560_{ex}/ 590_{em} nm) of resofurin at different time points (0, 24, 48, and 72 h). Error bars were calculated by taking the ratio between standard deviation of the sample set and square root of the sample population (N = 18). Two-way ANOVA was performed (Origin, 8th ed.) to evaluate significant differences between the factor level means within a factor and for interactions between the factors of different sample sets.

Conflict of Interest: The authors declare no competing financial interest.

Acknowledgment. This research was supported by a National Institutes of Health (NIH) Director's Pioneer Award (DP1OD003899) (D.H.M.D., J.H.L., T.W.O.) and the Center of Cancer Nanotechnology Excellence (CCNE) initiative of the NIH under Award Number U54 CA151880 (P.N.S., T.W.O.). Femtosecond laser studies (D.T.C., M.R.W.) were supported as part of the ANSER Center, an Energy Frontier Research Center funded by the U.S. Department of Energy, Office of Science, Office of Basic Energy Sciences, under Award Number DE-SC0001059. We thank Eunah You for initial TEM images of the gold nanostars, Keith Macrenaris for advice in cell culturing and biological assays, and Charlene Wilke for processing samples for TEM. Confocal imaging and metal analysis were performed at the Northwestern University Quantitative Bioelemental Imaging Center supported by National Science Foundation CHE-9810378/005 and NASA Ames Research Center NNA06CB93G. Biological assays were carried out in the High Throughput Analysis Laboratory, and dynamic light scattering and UV−vis spectroscopic measurements were performed at the NU Keck Biophysics Facility supported by Cancer Center Support Grant (NCI CA060553). HRTEM experiments were conducted at the Biological Imaging Facility. The authors also thank the staff in the Tumor Biology Core and the Robert H. Lurie Comprehensive Cancer Center Flow Cytometry Core for assistance.

Supporting Information Available: Optical properties of AuNS and structure of the aptamers; TEM images of Apt−AuNS located near NE folding; TEM images of changes in nuclear phenotype based on incubation times; TEM comparison of HeLa cell nuclei after treatment with free AS1411 and free control aptamer; flow cytometry and fluorescence characterization of aptamer released from gold nanostars in cancer cells after laser irradiation; confocal images of double-stranded DNA breaks (DSBs) of HeLa cells before and after light-triggered release of aptamers; comparison of caspase 3 and 7 activities of HeLa cells after various treatments; comparison of viability of HeLa cells after various treatments. This material is available free of charge *via* the Internet at http://pubs.acs.org.

REFERENCES AND NOTES

1. Zink, D.; Fischer, A. H.; Nickerson, J. A. Nuclear Structure in Cancer Cells. *Nat. Rev. Cancer* **2004**, *4*, 677–687.
2. Torchilin, V. P. Recent Approaches to Intracellular Delivery of Drugs and DNA and Organelle Targeting. *Annu. Rev. Biomed. Eng.* **2006**, *8*, 343–375.
3. Schwartz, G. K.; Shah, M. A. Targeting the Cell Cycle: A New Approach to Cancer Therapy. *J. Clin. Oncol.* **2005**, *23*, 9408–9421.
4. Ashkenazi, A. Targeting Death and Decoy Receptors of the Tumour-Necrosis Factor Superfamily. *Nat. Rev. Cancer* **2002**, *2*, 420–430.
5. Douglas, T.; Young, M. Viruses: Making Friends with Old Foes. *Science* **2006**, *312*, 873–875.
6. Bertoletti, A.; Gehring, A. J. The Immune Response during Hepatitis B Virus Infection. *J. Gen. Virol.* **2006**, *87*, 1439–1449.
7. Kay, M. A.; Glorioso, J. C.; Naldini, L. Viral Vectors for Gene Therapy: The Art of Turning Infectious Agents into Vehicles of Therapeutics. *Nat. Med.* **2001**, *7*, 33–40.
8. Rosi, N. L.; Giljohann, D. A.; Thaxton, C. S.; Lytton-Jean, A. K. R.; Han, M. S.; Mirkin, C. A. Oligonucleotide-Modified Gold Nanoparticles for Intracellular Gene Regulation. *Science* **2006**, *312*, 1027–1030.
9. Tkachenko, A. G.; Xie, H.; Coleman, D.; Glomm, W.; Ryan, J.; Anderson, M. F.; Franzen, S.; Feldheim, D. L. Multifunctional Gold Nanoparticle−Peptide Complexes for Nuclear Targeting. *J. Am. Chem. Soc.* **2003**, *125*, 4700–4701.
10. Oyelere, A. K.; Chen, P. C.; Huang, X.; El-Sayed, I. H.; El-Sayed, M. A. Peptide-Conjugated Gold Nanorods for Nuclear Targeting. *Bioconjugate Chem.* **2007**, *18*, 1490–1497.
11. Kang, B.; Mackey, M. A.; El-Sayed, M. A. Nuclear Targeting of Gold Nanoparticles in Cancer Cells Induces DNA Damage, Causing Cytokinesis Arrest and Apoptosis. *J. Am. Chem. Soc.* **2010**, *132*, 1517–1519.
12. Borer, R. A.; Lehner, C. F.; Eppenberger, H. M.; Nigg, E. A. Major Nucleolar Proteins Shuttle between Nucleus and Cytoplasm. *Cell* **1989**, *56*, 379–390.
13. Ginisty, H.; Sicard, H.; Roger, B.; Bouvet, P. Structure and Functions of Nucleolin. *J. Cell Sci.* **1999**, *112*, 761–772.
14. Soundararajan, S.; Wang, L.; Sridharan, V.; Chen, W. W.; Courtenay-Luck, N.; Jones, D.; Spicer, E. K.; Fernandes, D. J. Plasma Membrane Nucleolin Is a Receptor for the Anticancer Aptamer AS1411 in MV4-11 Leukemia Cells. *Mol. Pharmacol.* **2009**, *76*, 984–991.
15. Hovanessian, A. G.; Soundaramourty, C.; El Khoury, D.; Nondier, I.; Svab, J.; Krust, B. Surface Expressed Nucleolin Is Constantly Induced in Tumor Cells To Mediate Calcium-Dependent Ligand Internalization. *PLOS One* **2010**, 5.
16. Chen, X.; Kube, D. M.; Cooper, M. J.; Davis, P. B. Cell Surface Nucleolin Serves as Receptor for DNA Nanoparticles Composed of PEGylated Polylysine and DNA. *Mol. Ther.* **2007**, *16*, 333–342.
17. Nimjee, S. M. Aptamers: An Emerging Class of Therapeutics. *Annu. Rev. Med.* **2005**, *56*, 555–565.
18. Soundararajan, S.; Chen, W. W.; Spicer, E. K.; Courtenay-Luck, N.; Fernandes, D. J. The Nucleolin Targeting Aptamer AS1411 Destabilizes Bcl-2 Messenger RNA in Human Breast Cancer Cells. *Cancer Res.* **2008**, *68*, 2358–2365.
19. Bates, P. J.; Laber, D. A.; Miller, D. M.; Thomas, S. D.; Trent, J. O. Discovery and Development of the G-Rich Oligonucleotide AS1411 as a Novel Treatment for Cancer. *Exp. Mol. Pathol.* **2009**, *86*, 151–164.
20. Cao, Z.; Tong, R.; Mishra, A.; Xu, W.; Wong, G. C.; Cheng, J.; Lu, Y. Reversible Cell-Specific Drug Delivery with Aptamer-Functionalized Liposomes. *Angew. Chem., Int. Ed.* **2009**, *48*, 6494–6498.
21. Xie, J. P.; Lee, J. Y.; Wang, D. I. C. Seedless, Surfactantless, High-Yield Synthesis of Branched Gold Nanocrystals in HEPES Buffer Solution. *Chem. Mater.* **2007**, *19*, 2823–2830.
22. Demers, L. M.; Mirkin, C. A.; Mucic, R. C.; Reynolds, R. A., III; Letsinger, R. L.; Elghanian, R.; Viswanadham, G. A Fluorescence-Based Method for Determining the Surface Coverage and Hybridization Efficiency of Thiol-Capped Oligonucleotides Bound to Gold Thin Films and Nanoparticles. *Anal. Chem.* **2000**, *72*, 5535–5541.
23. Ma, L. L.; Tam, J. O.; Willsey, B. W.; Rigdon, D.; Ramesh, R.; Sokolov, K.; Johnston, K. P. Selective Targeting of Antibody Conjugated Multifunctional Nanoclusters (Nanoroses) to Epidermal Growth Factor Receptors in Cancer Cells. *Langmuir* **2011**, *27*, 7681–7690.

24. Hovanessian, A. G.; Puvion-Dutilleul, F.; Nisole, S.; Svab, J.; Perret, E.; Deng, J. S.; Krust, B. The Cell-Surface-Expressed Nucleolin Is Associated with the Actin Cytoskeleton. *Exp. Cell Res.* **2000**, *261*, 312–328.
25. Boisselier, E.; Astruc, D. Gold Nanoparticles in Nanomedicine: Preparations, Imaging, Diagnostics, Therapies and Toxicity. *Chem. Soc. Rev.* **2009**, *38*, 1759–1782.
26. Kim, J. A.; Aberg, C.; Salvati, A.; Dawson, K. A. Role of Cell Cycle on the Cellular Uptake and Dilution of Nanoparticles in a Cell Population. *Nat. Nanotechnol.* **2011**, *7*, 62–68.
27. Fricker, M.; Hollinshead, M.; White, N.; Vaux, D. Interphase Nuclei of Many Mammalian Cell Types Contain Deep, Dynamic, Tubular Membrane-Bound Invaginations of the Nuclear Envelope. *J. Cell Biol.* **1997**, *136*, 531–544.
28. Goulbourne, C. N.; Vaux, D. J. HIV Protease Inhibitors Inhibit FACE1/ZMPSTE24: A Mechanism for Acquired Lipodystrophy in Patients on Highly Active Antiretroviral Therapy? *Biochem. Soc. Trans.* **2010**, *38*, 292–296.
29. Ireson, C. R.; Kelland, L. R. Discovery and Development of Anticancer Aptamers. *Mol. Cancer Ther.* **2006**, *5*, 2957–2962.
30. Reyes-Reyes, E. M.; Teng, Y.; Bates, P. J. A New Paradigm for Aptamer Therapeutic AS1411 Action: Uptake by Macropinocytosis and Its Stimulation by a Nucleolin-Dependent Mechanism. *Cancer Res.* **2010**, *70*, 8617–8629.
31. Wijaya, A.; Schaffer, S. B.; Pallares, I. G.; Hamad-Schifferli, K. Selective Release of Multiple DNA Oligonucleotides from Gold Nanorods. *ACS Nano* **2009**, *3*, 80–86.
32. Jain, P. K.; Qian, W.; El-Sayed, M. A. Ultrafast Cooling of Photoexcited Electrons in Gold Nanoparticle-Thiolated DNA Conjugates Involves the Dissociation of the Gold–Thiol Bond. *J. Am. Chem. Soc.* **2006**, *128*, 2426–2433.
33. Huschka, R.; Zuloaga, J.; Knight, M. W.; Brown, L. V.; Nordlander, P.; Halas, N. J. Light-Induced Release of DNA from Gold Nanoparticles: Nanoshells and Nanorods. *J. Am. Chem. Soc.* **2011**, *133*, 12247–12255.
34. Yavuz, M. S.; Cheng, Y.; Chen, J.; Cobley, C. M.; Zhang, Q.; Rycenga, M.; Xie, J.; Kim, C.; Song, K. H.; Schwartz, A. G. Gold Nanocages Covered by Smart Polymers for Controlled Release with Near-Infrared Light. *Nat. Mater.* **2009**, *8*, 935–939.
35. Hill, H. D.; Millstone, J. E.; Banholzer, M. J.; Mirkin, C. A. The Role Radius of Curvature Plays in Thiolated Oligonucleotide Loading on Gold Nanoparticles. *ACS Nano* **2009**, *3*, 418–424.
36. Anger, P.; Bharadwaj, P.; Novotny, L. Enhancement and Quenching of Single-Molecule Fluorescence. *Phys. Rev. Lett.* **2006**, *96*, 113002.
37. Rogakou, E. P.; Pilch, D. R.; Orr, A. H.; Ivanova, V. S.; Bonner, W. M. DNA Double-Stranded Breaks Induce Histone H2AX Phosphorylation on Serine 139. *J. Biol. Chem.* **1998**, *273*, 5858–5868.